

Petro-electric modeling for CSEM reservoir characterization and monitoring

Alireza Shahin¹, Kerry Key², Paul Stoffa³, and Robert Tatham⁴

ABSTRACT

The controlled-source electromagnetic (CSEM) method has been successfully applied to petroleum exploration; however, less effort has been made to highlight the applicability of this technique for reservoir monitoring. This work appraises the ability of time-lapse CSEM data to detect the changes in fluid saturation during water flooding into an oil reservoir. We simulated a poorly consolidated shaly sandstone reservoir based on a prograding near-shore depositional environment. Starting with an effective porosity model simulated by Gaussian geostatistics, dispersed clay and dual water models were efficiently combined with other well-known theoretical and experimental petrophysical correlations to consistently simulate reservoir properties. The constructed reservoir model was subjected

to numerical simulation of multiphase fluid flow to predict the spatial distributions of fluid pressure and saturation. A geologically consistent rock physics model and a modified Archie's equation for shaly sandstones were then used to simulate the electrical resistivity, showing up to 60% decreases in electrical resistivity due to changes in water saturation during 10 years of production. Time-lapse CSEM data were simulated at three production time steps (zero, five, and ten years) using a 2.5D parallel adaptive finite element algorithm. Analysis of the time-lapse signal in the simulated multicomponent and multifrequency data set demonstrates that a detectable time-lapse signal after five years and a strong time-lapse signal after ten years of water flooding are attainable using current CSEM technology.

INTRODUCTION

The CSEM method has been recently applied to petroleum exploration as a direct hydrocarbon detector. The contrast between the low electrical conductivity of hydrocarbon-saturated rocks and the higher conductivity of the surrounding water-saturated rocks leads to an anomaly in the magnetic and electric fields emitted in the vicinity of the sea floor by electric dipole transmitters and recorded by ocean bottom EM receivers. Successful applications are documented in several studies (e.g., Ellingsrud et al., 2002; Eidesmo et al., 2002; Constable and Srnka, 2007).

Time-lapse CSEM data consist of two or more repeat surveys recorded at different calendar times over a depleting reservoir. The main objective is to detect and estimate production-induced time-lapse changes in subsurface rock and fluid properties. In doing so, changes in observations, i.e., the amplitude and phase of

magnetic and electric fields, or inverted attributes, e.g., rock resistivity, can be associated to changes in fluid saturation assuming a noncompacting isothermal reservoir.

Time-lapse CSEM has been considered by several authors in the literature. Wright et al. (2002) present time-lapse transient EM surveys over a shallow underground gas storage reservoir and demonstrated that the data are repeatable enough to detect the reservoir and monitor the evolution of the gas and water content. Lien and Mannseth (2008) conduct a feasibility study of time-lapse CSEM data to monitor the water flooding of an oil reservoir. Utilizing 3D integral equation modeling, they find that time-lapse signals exhibit detectable changes even in the presence of measurement errors. Orange et al. (2009) utilize 2D finite element modeling to simulate time-lapse CSEM data for several simplified water flooding scenarios. Through a set of 2D modeling studies, they show that a data

Manuscript received by the Editor 11 October 2010; revised manuscript received 11 July 2011; published online 3 February 2012.

¹Formerly University of Texas at Austin, Institute for Geophysics, Austin, Texas, USA. Presently BP North America Inc., Reservoir Geophysics R&D, Houston, Texas, USA. E-mail: alireza.shahin@bp.com.

²Scripps Institution of Oceanography, University of California, San Diego, California, USA. E-mail: kkey@ucsd.edu.

³University of Texas, Institute for Geophysics, Austin, Texas, USA. E-mail: pauls@ut.ig.utexas.edu.

© 2012 Society of Exploration Geophysicists. All rights reserved.

repeatability of 1%–2% relative error is required to detect the small time-lapse signals. Zach et al. (2009) conduct 3D time-lapse modeling by perturbing conductivity over a large reservoir ($10 \times 10 \text{ km}^2$) and report changes of 30% to 50% in relative amplitudes of base and monitor surveys. Black et al. (2009) models the time-lapse CSEM response over a realistic geologic model for a simplified flood geometry, but without fluid flow simulation and rock-physics modeling. They show that marine CSEM data are able to locate the position of the oil-water contact if the complicating effects from the background, bathymetry, and a salt dome are taken into account.

These previous studies used direct perturbation of electrical conductivity under the reasonable assumption that reservoir depletion will give substantial resistivity variations, rather than using reservoir simulation and rock-physics modeling to determine the expected resistivity changes. Ziolkowski et al. (2010) published a time-domain EM repeatability experiment over the North Sea Harding field where fluid flow simulation and resistivity modeling by Archie's equation for clay-free sandstone were combined by integral equation modeling to simulate the observed EM data. They concluded that the production-induced time-lapse changes in reser-

voir resistivity would be observable provided that a signal to noise ratio of greater than 100, i.e., 40 dB, is obtained.

Here, we generate a 2D geological reservoir model that exhibits a realistic spatial distribution of petrophysical properties. Fluid flow simulation and a geologically consistent rock-physics model are then employed to convert the petrophysical properties of the shaly sandstone to electrical resistivity. The representative time-dependent resistivity model developed here shows an accurate front geometry during water flooding. To simulate the surrounding rocks, we bury the reservoir into a 1D background resistivity model. We then numerically acquire 2.5D time-lapse CSEM data over the reservoir to assess the value of EM data in monitoring a complicated water-flooding scenario.

CONSTRUCTING A SYNTHETIC RESERVOIR MODEL

Geological reservoir model

A stacked sand-rich strandplain reservoir architecture is considered in this study to simulate a realistic geological framework.

Strandplains are mainly marine-dominated depositional systems generated by seaward accretion of successive, parallel beach ridges welded onto the subaerial coastal mainlands. They are inherently progradational features and are present on wave-dominated microtidal coasts (Tyler and Ambrose, 1986; Galloway and Hobday, 1996). This sand-rich beach-ridge reservoir architecture is inferred to be originally deposited as a clay-free geobody. However, due to postdepositional diagenesis, dispersed clay is produced and it is the main factor reducing porosity and permeability of the reservoir. This model, generated using a Gaussian simulation technique, is part of the Comparative Solution Project, a widely used, large geostatistical model for research on upgridding and upscaling approaches (Christie and Blunt, 2001). We worked with the top 35 layers of the model, which are representative of the Tarbert formation, a part of the Brent sequence of middle Jurassic age and one of the major producers in the North Sea. By changing the grid size and imposing smoothness, we modified this model to meet the objectives of this research. Next, we assigned geologically consistent petrophysics information and add facies characterization to develop a more realistic reservoir model comparable to complicated models in the petroleum industry. The model is described on a regular Cartesian grid. The model size is $220 \times 60 \times 35$ cells in the X (east-west), Y (north-south), and Z (depth) directions, respectively. The grid size is $10 \times 10 \times 10 \text{ m}$, giving total model dimensions of $2200 \times 600 \times 350 \text{ m}$.

The reservoir consists of three facies (Figure 1). Facies A is a fine grained sandstone with mean grain size distribution of $80 \mu\text{m}$. This facies simulates a low porous and permeable sandstone reservoir with high clay content. Facies C is a course grained sandstone with mean

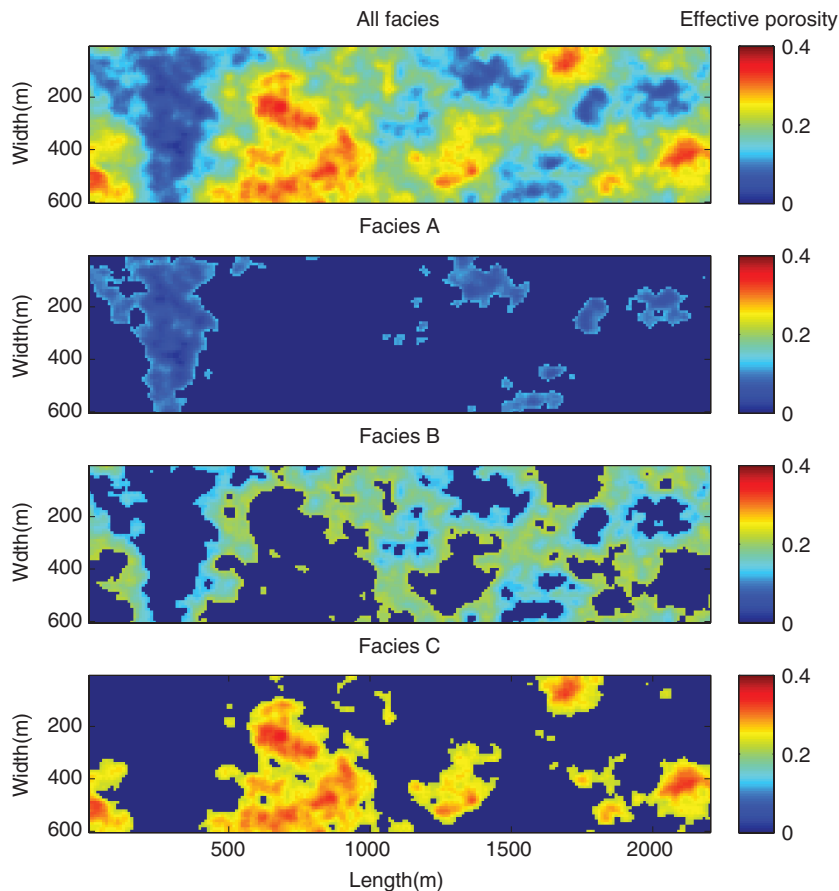


Figure 1. Map view of the first upper layer of the 3D reservoir (Christie and Blunt, 2001) showing petrophysical facies (A, B, and C) overlaid on the distribution of effective porosity model. Color scale is effective porosity and the same for all panels. The model is associated with synthetic geologic model and used for the numerical simulation of multiphase fluid flow, rock physics, and CSEM modeling. The model is defined on a regular Cartesian grid of $10 \times 10 \times 10 \text{ m}$ cells, with $220 \times 60 \times 35$ cells in X (east-west), Y (north-south), and Z (depth) directions, respectively, for a total dimension of $2200 \times 600 \times 350 \text{ m}$. A 2D cross section from the middle of this 3D model has been selected for this study.

grain size distribution of 500 μm . This facies is associated with a sandstone with high porosity and permeability and low clay content. Facies B is a transition facies between facies A and C and corresponds to a medium grained sandstone with mean grain size distribution of 250 μm . It is worth noting that a strong correlation between grain size and clay content is reported by several authors (e.g., Saner et al., 1996), so this knowledge has been accordingly incorporated into the model by assigning clay-dependent grain sizes to the three facies, i.e., the higher the clay content, the lower the mean grain size distribution.

Petrophysics model

The geological model described above is used to populate the petrophysical properties, assuming a meaningful petrophysics model. A petrophysics model includes the theoretical and experimental correlations among various sets of petrophysical properties. The model is required to be validated using available well log and core data. Here, the effective porosity model was first generated using Gaussian geostatistics and clay content, and total porosity models were then computed assuming a dispersed clay distribution (Thomas and Stieber, 1975; Marion et al., 1992), as shown in Figure 2a. Horizontal permeability in the X and Y directions are equal and calculated based on the extension of the dispersed clay model for permeability introduced by Revil and Cathles, 1999 (Figure 2b and 2c). It is worth mentioning that permeability fields depend on porosity, clay content, grain size distribution, and the degree of cementation; subsequently facies A, B, and C were assigned different trends in permeability-clay content and permeability-porosity domains based on their grain sizes (Table 1). The vertical permeability field was taken as 25% of the horizontal permeability field for the entire reservoir. It is worth mentioning that the joint relationship of permeability and resistivity has been taken into account by assigning three different cementation factors to the three facies.

So far, the effective and total porosities, clay content and directional permeabilities are modeled using geostatistics and theoretical correlations according to the dispersed clay distribution. Next, we initialize the reservoir for water saturation and pore pressure. An experimental correlation (Uden et al., 2004) between water

saturation and clay content was combined with the dual water model (Best et al., 1980; Dewan, 1983; Clavier, 1984) to compute clay bound-water (Swb), effective water saturation (Swe), total water saturation (Sw_t), and oil saturation (So) (Figure 2d and Table 1). Initial reservoir pore pressure was simulated assuming a linear hydrostatic gradient from the top to the bottom of the reservoir. Figure 3 summarizes the distribution of petrophysical properties for a 2D cross section in the middle of the 3D reservoir. This 2D reservoir has been used for the numerical simulation of multiphase fluid flow, rock physics, and CSEM modeling in this paper.

Reservoir simulation

Fluid flow simulation combines three fundamental laws governing fluid motions in porous media. These laws are based on conservation of mass, momentum, and energy (Aziz and Settari, 1979). In this research, the commercial finite difference reservoir simulator, Eclipse 100, is utilized to replicate a water flooding plan on a 2D

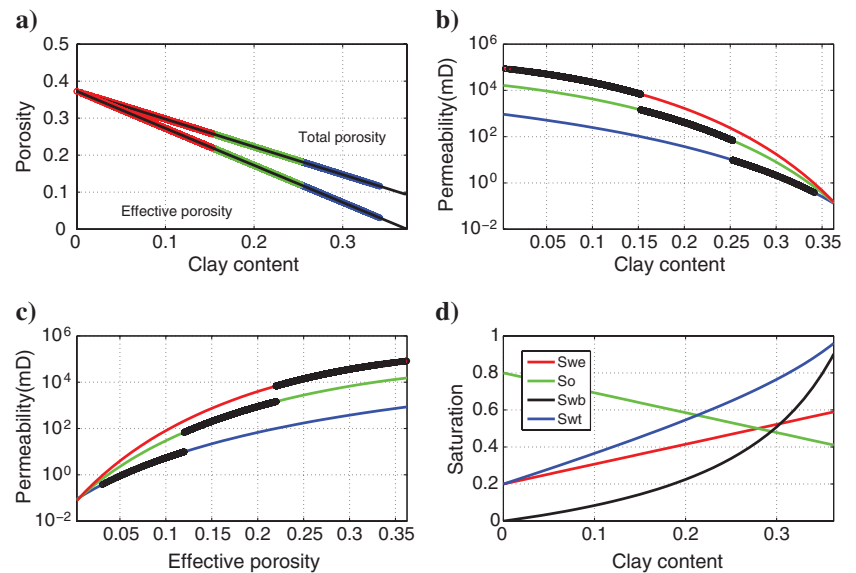


Figure 2. Petrophysics model. Panel (a) shows the dispersed clay model for porosity reduction due to increasing of clay. Panel (b) displays horizontal permeability versus clay content. Panel (c) is permeability vs. effective porosity. In panels (a), (b), and (c), three colors are associated with three facies A (in blue), B (in green), and C (in red). Black dots in panels (b) and (c) are projected reservoir points. Note that the high concentration of projected points looks like a continuous curve. Panel (d) shows fluid saturations vs. clay content. Swe, So, Swb, and Sw_t are effective water saturation, oil saturation, clay bound-water saturation, and total water saturation, respectively. Note that the summation of effective water saturation (red curve) and oil saturation (green curve) is always one.

Table 1. Facies petrophysical properties associated with the synthetic reservoir model.

Facies	Total porosity	Effective porosity	Clay content	Effective water saturation	Mean grain size(micron)	Horizontal permeability (mD)
A	0.11–0.18	0.01–0.12	0.25–0.34	0.45–0.62	80	0.37–10
B	0.18–0.25	0.12–0.22	0.15–0.25	0.27–0.45	250	68–1400
C	0.25–0.37	0.22–0.37	0.0–0.15	0.15–0.27	500	6800–91,000

reservoir containing oil, soluble gas, and water. The reservoir has no natural water drive. In addition, because of the high pressure conditions, no gas is produced in the reservoir. Thus, solution gas is the only drive mechanism forcing oil to be produced. This drive is so weak that implementation of water injection is required to enhance oil recovery. The same grid block dimensions used to generate the geological model, $10 \times 10 \text{ m}^2$, were used to simulate fluid flow; hence mathematical upscaling was not necessary.

The capillary pressure data, the relative permeability curves, and PVT (pressure, volume, and temperature) properties of reservoir fluids are borrowed from the well-known SPE 9th model (Killough, 1995) and slightly modified to meet research objectives. Based on this data, the pressure below which the dissolved gas releases from oil (the bubble point) is 2000 psi.

For a period of ten years, the waterflood schedule is simulated by using two injectors at the corners and one producer in the middle of the 2D reservoir (Figure 4). In this period, saturations and pressures values for each reservoir grid block are exported after each year. Collecting this database allows us to analyze the sensitivity of the corresponding rock resistivity and CSEM data to a wide range of changes in saturation. Figure 4 shows the snapshots of water saturation and pore pressure distributions for the initial reservoir state and after production at different calendar times. With the start of production/injection, oil is replaced by water near the injectors and the producer extracts a portion of mobile oil. Increasing the time, more oil is replaced with water, hence more oil has been produced. In other words, behind the waterfronts, the water saturation is increasing monotonically toward the injectors, meaning more oil is gradually displaced as more water is injected. In addition, one can clearly see that the behavior of the pressure front is very different from that of the waterfront. In fact, pressure has a wave motion like

behavior and propagates very fast, but water has a mass bulk movement and moves slowly.

Figure 5 illustrates surface reservoir simulation outputs, i.e., production data, for a period of ten years throughout the reservoir life. Water injectors perforate the entire 350 m of reservoir thickness and are set to a constant water rate of 400 STB/Day. The only producer located in the middle of reservoir also perforates the whole reservoir thickness and is initially set to a constant oil rate of 750 STB/Day. The reservoir initially starts producing oil with a plateau of 750 STB/Day. During this period, volumetric average pressure of the reservoir increases from 3200 to 3920 psi. After 2650 days, this rate is not affordable for the reservoir, so the production strategy is intentionally changed to a constant bottom hole pressure (BHP) of 2600 psi for the producer. From this point the oil rate will decrease and a significant pressure drop is observed. The reservoir always produces above the bubble point pressure, i.e., 2000 psi; consequently, no gas is produced within the reservoir. However, dissolved gas will be released from live oil at the surface and gas will be produced with a similar production trend as oil. A slight water production occurs from the beginning up to 2000 days of production, but it increases significantly afterward.

Rock and fluid physics model

Using rock-physics modeling, one can transform the petrophysical properties of a reservoir to rock resistivity, which can then be used to simulate CSEM data. This process is an essential step in any inversion project aimed at estimating petrophysical properties. For CSEM reservoir monitoring purposes, fluid flow simulation, rock-physics, and CSEM forward modeling can be effectively combined to simulate CSEM data and, ultimately, to predict reservoir properties through an inversion algorithm.

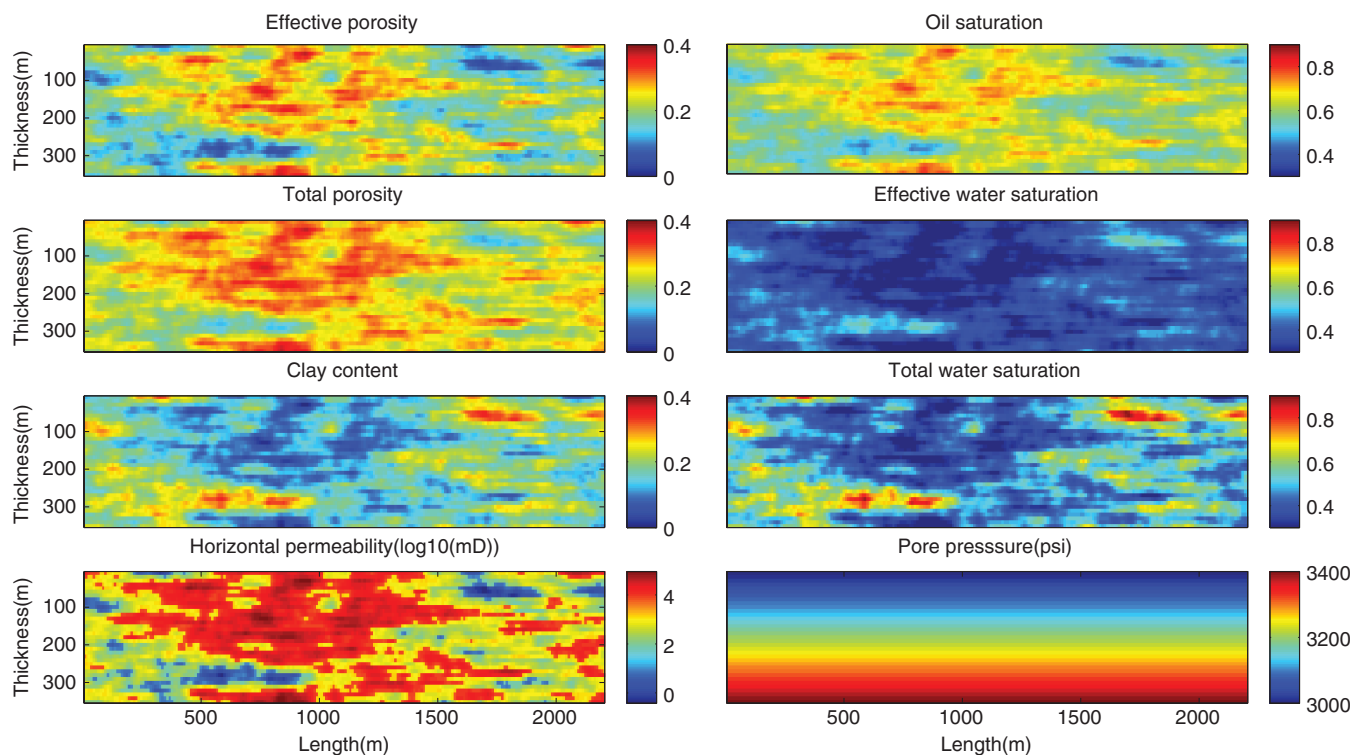


Figure 3. Distribution of petrophysical properties for a 2D cross section in the middle of the 3D reservoir.

Porosity in clastic rocks is controlled by two main factors. The first one is sedimentation, i.e., porosity variation resulting from variations in sorting and clay content. The second factor is diagenesis, i.e., porosity reduction due to pressure solution, compaction, and cementation (Avseth et al., 2005). Here, we deal with a strandplain geological architecture filled with poorly consolidated shaly sandstone. As described in the petrophysics model, the clay distribution is dispersed or pore-filling. The corresponding porosity-clay model was introduced by Thomas and Stieber (1975) and further developed by Marion et al. (1992). As mentioned earlier, the dispersed clay is the main factor reducing porosity and permeability of the reservoir.

Archie's equation (Archie, 1942) has been widely used in the geosciences community to relate petrophysical properties of reservoir rocks to electrical resistivity. However, this theory is not valid in shaly sandstones due to the excess conductivity of clay. Through the evolution of well log interpretation, several shaly sand resistivity models have been developed for different types of clay distribution, i.e., dispersed, structural, and laminated clays. Among these models, the Waxman-Smits model (Waxman and Smit, 1968) and dual water models (Best et al., 1980; Dewan, 1983; Clavier et al., 1984) are more applicable for dispersed clay distributions. In this study, we used the dual water model because several of its parameters can be computed from well logs (Dewan, 1983) and it can be efficiently combined with the dispersed clay model. Formation water resistivity depends on salinity and temperature. We used Arps' empirical equation (Arps, 1953) to calculate the free and bound-water resistivity. Appendix A summarizes the rock and fluid model employed.

Figure 6 summarizes the rock physics model employed. Panel (a) shows the effect of changes in porosity at constant water saturation on rock resistivity. As expected based on Archie's equation, resistivity decreases by increasing porosity. Panel (b) displays the effect of saturation at constant porosity or clay content on rock resistivity. Resistivity decreases by increasing water saturation because of the conductivity of saline water.

The corresponding petro-elastic model for the reservoir can be simulated by combining the Thomas and Stieber (1975) petrophysics model, the Dvorkin-Gutierrez (2002) rock-physics model, the

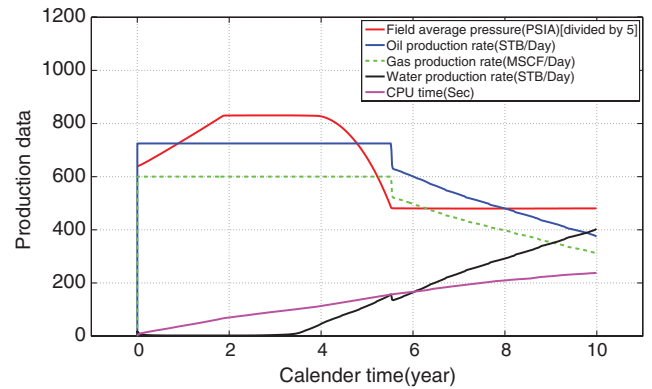


Figure 5. Surface reservoir simulation outputs, i.e., production data, for a period of ten years of water flooding to enhance oil recovery.

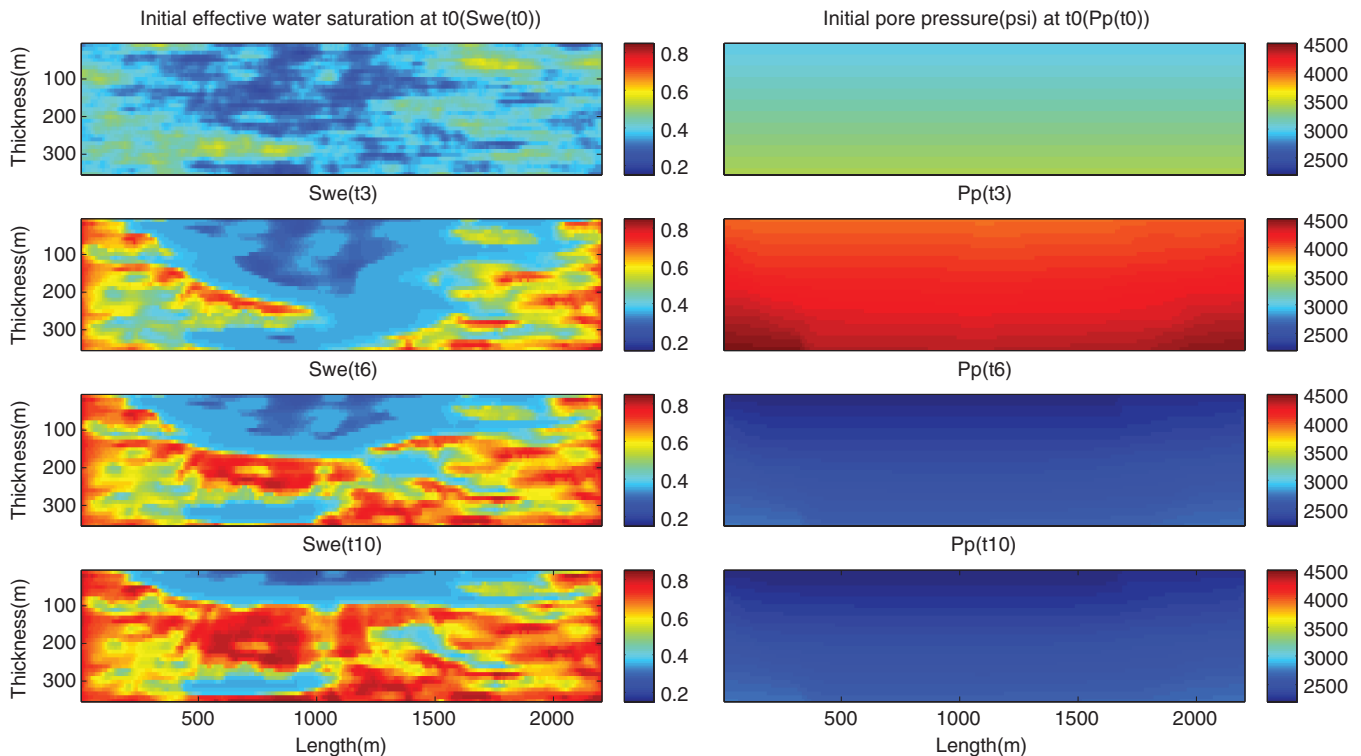


Figure 4. Snapshots of effective water saturation and pore pressure (psi) distributions at initial reservoir state (t_0) and after production at different calendar times (three [t_3], six [t_6], and ten [t_{10}] years). X and Y axes are the same for all panels and they are reservoir length and thickness in meters, respectively. Each panel is color-coded for the corresponding attribute. Two water injectors and one producer are located in the corners and in the middle of the 2D reservoir, respectively.

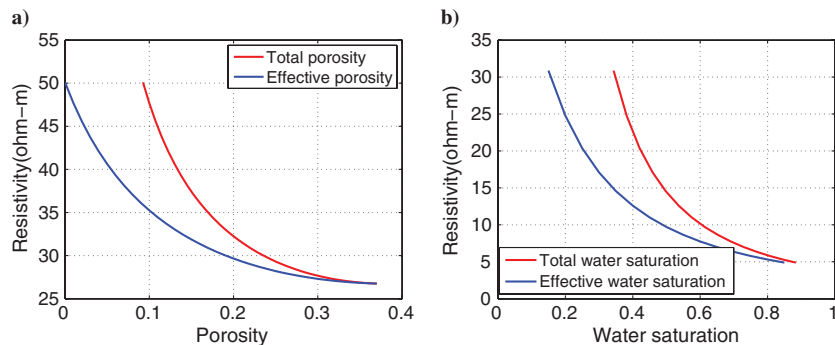


Figure 6. Rock physics model displaying the effects of porosity at constant effective water saturation of 0.5 (a) and saturation at constant effective porosity of 0.2 (b) on rock resistivity.

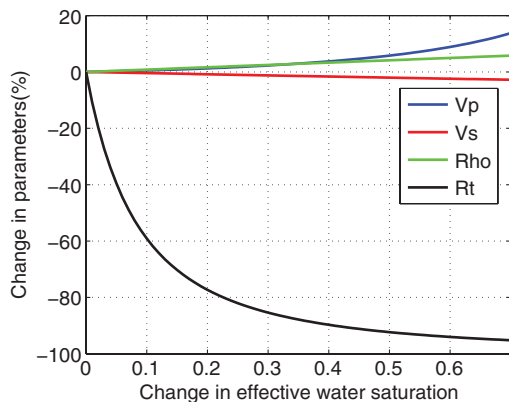


Figure 7. Comparison of seismic and CSEM rock-physics model in terms of time-lapse signal due to changes in effective water saturation. Elastic parameters including P-wave velocity (V_p), S-wave velocity (V_s), and density (Rho) are less affected than rock resistivity (R_t).

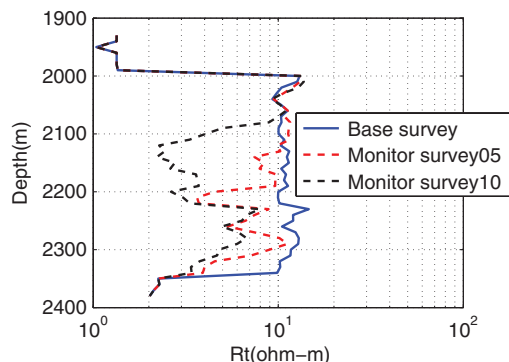


Figure 8. Resistivity logs extracted from the middle of the 2D reservoir for base survey (blue), the first monitor survey after five years of water flooding (dashed red), and the second monitor survey after ten years of water flooding (dashed black).

fluid physics model (Batzie and Wang, 1992), and a modified Gassmann theory (Dvorkin et al., 2007) for shaly sandstones. The joint modeling of the elastic and electrical properties of reservoir rocks will lead to the consistent forward modeling algorithm for joint inversion of seismic and CSEM data and is a topic for future research. Further applications of using the petro-elastic model can be found in Shahin et al. (2010, 2011).

The surrounding offshore sedimentary basin in which the reservoir is buried is replicated using a 1D resistivity model generated by correlating the P-wave velocity and resistivity based on the modified Faust equation (Hacikoylu et al., 2006). Because the fine detailed structure of the overburden is irrelevant to the time-lapse studies considered here, we then simplified this into a two layer model with 1.5 and 2.5 ohm-m layers separated by a contact at 2350 m below sea surface (the same depth as the base of the reservoir). A 1 km thick, 0.33 ohm-m layer represents the overlying conductive ocean.

Figure 7 compares the seismic and CSEM rock-physics models in terms of their time-lapse signals due to changes in effective water saturation. By increasing the effective water saturation, rock resistivity (R_t) changes significantly, about 100%, but elastic parameters including P-wave velocity (V_p), S-wave velocity (V_s), and density (Rho) are all less affected, e.g., at most 14%.

Figure 8 illustrates three resistivity logs extracted from the middle of the 2D reservoir in the vicinity of the producer. These are related to the base case (t_0) before water flooding and two monitor surveys (t_{05} and t_{10} , i.e., after five and ten years of water flooding, respectively). As expected, resistivity decreases as injected saline water replaces oil. Note that the absolute values of the resistivity, less than 10 ohm-m, are significantly lower than that of the simple “canonical” reservoir considered in many previous studies (e.g., Constable and Weiss, 2006; Key, 2009), in which reservoirs of 100 ohm-m electrical resistivity and 100 m thickness are investigated. This fact is due to the excess conductivity of clay and makes our reservoir seemingly a more difficult-exploration target. However it is also worth noting that CSEM is predominantly sensitive to the resistivity-thickness product of the reservoir (e.g., Constable and Weiss, 2006). While the reservoir considered here has a resistivity of only 10 ohm-m, its thickness of 300 m results in a resistivity-thickness product only about a factor of three lower than for the canonical reservoir, therefore making it a good exploration target. Now, the key question is whether or not the time-lapse reservoir changes are also a good target for monitoring.

Figure 9 displays the percentage of time-lapse changes in effective water saturation and the associated changes in rock resistivity and seismic acoustic impedance. Here, for any parameter the base survey value is subtracted from that of the monitor survey and then normalized using that of the base survey. For plotting the changes in resistivity, a minus sign is applied to have a consistent color display for flood geometry between saturation, acoustic impedance, and resistivity models. As confirmed in Figure 7, resistivity is much more sensitive to water saturation than acoustic impedance.

CSEM MODELING

The changes in the reservoir resistivity shown in Figure 9 are substantial; however, we expect the corresponding changes in

the measured CSEM data to be much smaller due to the inherent sensitivity scaling of low frequency EM data. To accurately model these small changes, we utilized a recently developed finite element code for simulating frequency domain CSEM data in 2.5D (Key and Ovall, 2011). This is a parallel code that makes use of several recently developed approaches to enhance the performance of finite element methods. A fully unstructured triangular element grid is implemented to handle earth structures with an arbitrary level of 2D complexity. A sparse-direct matrix factorization is used to rapidly solve the linear systems with multiple right hand-side vectors associated with multiple EM transmitters. An automated adaptive mesh refinement algorithm is employed, which starts from a coarse grid and uses an a posteriori finite element error estimator to iteratively guide grid refinement until the desired solution accuracy has been obtained. Specifically, this code uses a dual-weighted residual approach for the error estimator, which has been found to be more robust than the gradient-based error estimator proposed previously in Li and Key (2007). The adaptive refinement computations are divided so that the code is parallelized over subsets of the input parameters (transmitters, frequencies, and 2.5D Fourier wavenumbers), thereby allowing for efficient scaling on parallel computers containing up to about one thousand processors. Further details can be found in Key and Ovall (2011).

An example of the coarse starting grid used for the finite element computations is shown in Figure 10. Here the multiscale benefits of the unstructured grid are readily apparent. Elements in the reservoir region are constrained to have an area of about 50 m^2 , while elements outside the reservoir region have no area constraint. In this way, the unstructured model grid only contains fine detail in the desired regions, thereby resulting in an efficient use of mesh nodes. Conversely, the structured rectangular grids typically used for finite difference and finite element meshes would have thin rows and

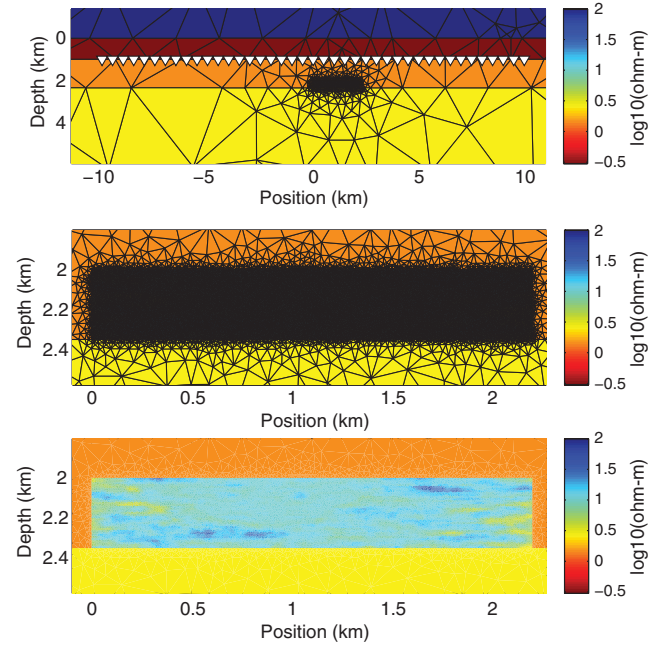


Figure 10. Triangular mesh of electrical resistivity used as the coarse starting grid for the adaptive finite element CSEM computations. Elements in the reservoir have a cross-sectional area of about 50 m^2 . The top panel shows a wide view of the central region, illustrating how an unstructured grid can efficiently handle multiple scale conductivity features. The middle and bottom panels show a close up view of the reservoir region (for the base model before water flooding) with and without the mesh edges. White triangles show the locations of the 41 EM receivers along the seafloor.

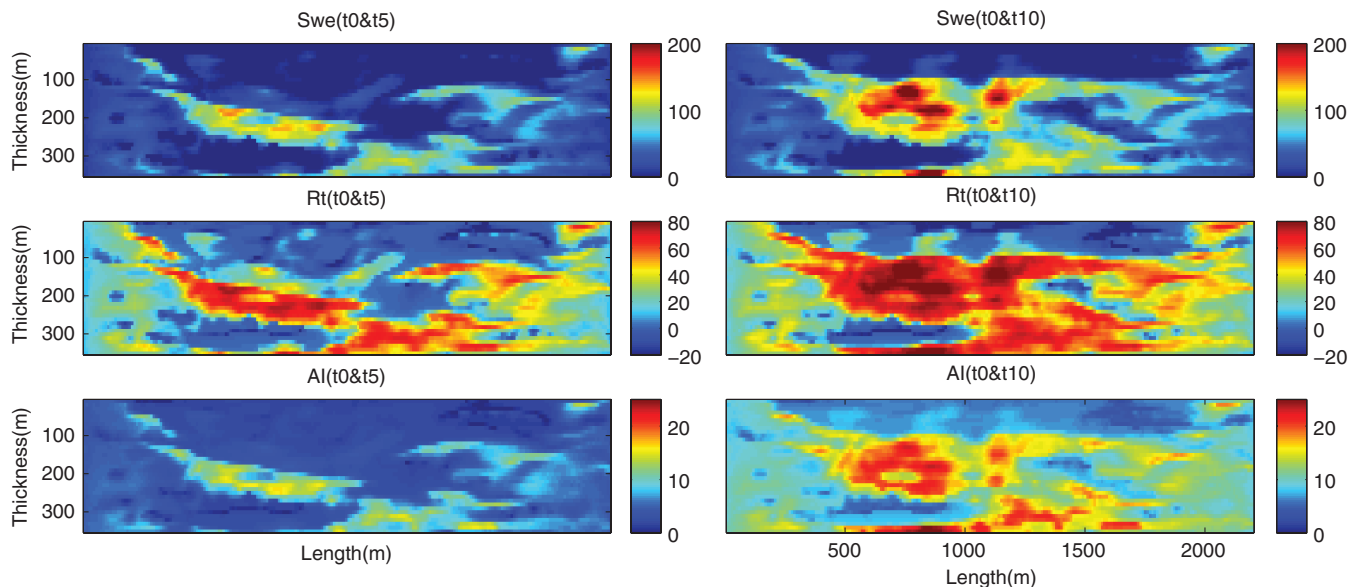


Figure 9. Time-lapse percentage changes in effective water saturation and the associated changes in electrical resistivity and seismic acoustic impedance for the first monitor survey (left column) and the second monitor survey (right column) after five and ten years of water flooding, respectively. X and Y axes are the same for all panels and they are reservoir length and thickness in meters, respectively. Each panel is color-coded for the corresponding attribute. As mentioned in text, a minus sign is applied on the resistivity to have a consistent color display for flood geometry between saturation, acoustic impedance, and resistivity models.

columns that extend laterally and vertically away from the reservoir region all the way to the model edges, thereby resulting in a significant increase in the number of mesh nodes and hence an unnecessarily larger linear system to solve. After the finite element grid was generated, the resistivity of each triangle in the reservoir region was assigned to the nearest 10×10 m cell from the corresponding reservoir modeling grid, resulting in CSEM modeling grids for the base case and for five and ten years of water flooding.

In the numerical simulations, we employed 41 inline electric dipole transmitters positioned 20 m above the sea bed, and 41 receivers located on the sea bed, all equally spaced every 500 m. Since CSEM data are typically collected using a transmitter waveform containing a broad bandwidth of discrete frequency harmonics (e.g., Myer et al., 2011), we modeled frequencies of 0.1, 0.3, 0.5 and 0.7 Hz. While the code outputs all field components, here we only examine the three fundamental components for an inline transmitter (the crossline magnetic field, and the inline and vertical electric fields). As demonstrated by previous studies, employing multicomponent and multifrequency measurements in interpretation and inversion of CSEM data can lead to better reservoir characterization (e.g., Um and Alumbaugh, 2007; Key, 2009).

The adaptive finite element procedure was set to run until the solution obtained an estimated accuracy no worse than 0.3%

relative error. The coarse starting grid used 13,826 mesh nodes while the finally refined grids required between 70,000–110,000 nodes to achieve the requested 0.3% accuracy, depending on the specific parameters of the parallel refinement tasks. Computations were performed using 960 processors on a parallel cluster computer, taking about 90 s total per time-lapse model. For comparison, only 55 s was required to obtain 1% accuracy and 34 s was required for 10% accuracy.

Figure 11 shows an example of the CSEM responses for the base case before any water flooding. To establish a baseline signal of the reservoir signal (c.f., the time-lapse signal) responses are shown for a “reference” off-target receiver at position -10 km and a target receiver near the edge of the reservoir at -1 km position. As expected, the target receiver has significantly larger amplitudes than the off-target receiver. The CSEM anomalies (relative difference between the target and off-target responses) for all field components are largest at the highest frequency (0.7 Hz) with 50%–150% anomalies, whereas at the lowest frequency (0.1 Hz) the anomalies are only about 10%–20%, depending on the particular field component.

The amplitude decay curves show that the fields intersect typical CSEM acquisition system noise floors of 10^{-19} – 10^{-18} T/Am and 10^{-16} – 10^{-15} V/Am² (e.g., Constable and Weiss, 2006; Hoversten

et al., 2006) at ranges of about 7 km for 0.7 Hz to greater than 12 km for 0.1 Hz. The peak anomalies occur at 3–7 km ranges. An exception is the large second peak in the inline electric field at about 8 km range. Examination of the amplitude plot shows that this secondary peak is related to the arrival of the airwave, which results in a local amplitude minimum where the upward and downward traveling energy have similar magnitudes but opposite phase, leading to a field cancellation (e.g., Orange et al., 2009). While fundamentally interesting from a physical standpoint, this phenomenon occurs at amplitudes around the system noise level and we therefore consider it less relevant than the primary anomalies at 3–7 km range. The crossline magnetic field also shows a change in decay rate at longer ranges associated with the airwave but does not contain the local amplitude minimum; the vertical electric field shows no signs of the airwave, as expected based on previous studies.

Now that we have established the baseline reservoir signal of 10%–50% anomalies, we can compare that to the time-lapse signals generated from water flooding. Instead of showing line plots, we condense the data from all 41 transmitters and receivers into simple 2D sections. This is accomplished by plotting the anomaly (here the relative difference between the water-flooded model and the base model) horizontally at the transmitter-receiver midpoint and vertically at the transmitter-receiver offset (range). Since the CSEM fields generally become more sensitive to depth with increasing offset, the vertical axis can be thought of as relative depth scale. These anomaly midpoint-offset sections are shown in

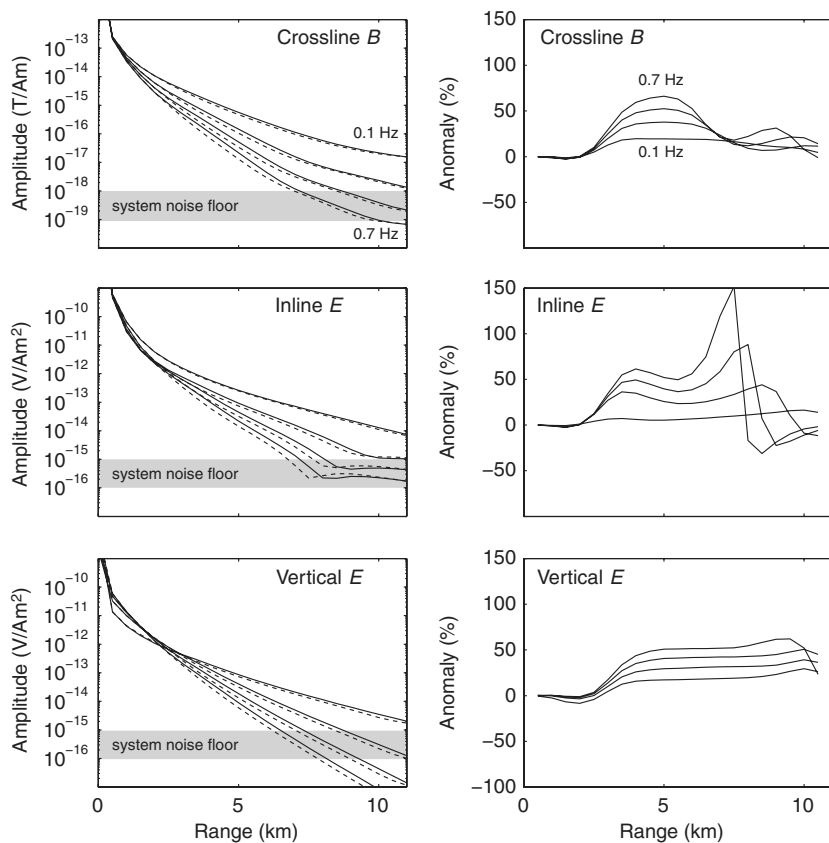


Figure 11. CSEM responses of the base model (before water flooding) shown in Figure 10 for various frequencies (0.1, 0.3, 0.5, and 0.7 Hz). The left column shows the magnetic and electric field amplitude responses for the three fundamental components (crossline, inline, and vertical) for a receiver located far off the reservoir at position -10 km (dashed line) and near the edge of the reservoir at position -1 km (solid line). Responses are shown for transmitter tows to the right of the receiver. The right column shows the anomaly (relative difference) between the two receivers.

Figures 12, 13, and 14 for the crossline magnetic field and the inline and vertical electric fields, computed for five and ten years flooding.

Again we see that the peak anomalies occur for the highest frequency, but now we can see that the anomalies are largely confined to data with transmitter-receiver midpoints located over the reservoir (position 0–2.2 km). Since the water flooding leads to a decrease in resistivity, the anomalies are generally negative. The location and shape of the anomalies is fairly similar among the three field components, yet the vertical electric field has a significant positive anomaly at shorter offsets. This is likely due to a change in the vertical electrical impedance of the reservoir during water flooding, leading to a galvanic distortion of electric current flowing normal to the top boundary. This is supported by the observation that this effect is largest at the lowest frequency, where galvanic effects are expected to be more significant than inductive effects. Contours of the system noise floor show that most of the anomalies are present at shorter offsets and are therefore observable with existing survey gear.

After five years of flooding, the negative anomalies are only about -1% at 0.1 Hz and about -5% at 0.7 Hz. After ten years of flooding much larger anomalies are observed: about -5% at 0.1 Hz and -10% at 0.7 Hz. Given the 50% anomaly for the base reservoir when compared with an off-target receiver, these 5%–10% time-lapse signals represent fairly significant anomalies. Since the data repeatability for a real survey is likely to be at best about 1%–2% using currently available nodal CSEM receivers and a deep-towed transmitter, the -5% anomaly associated with five years of water flooding would be just detectable, but the -10% anomaly after ten years of water flooding should be more readily detectable with existing CSEM survey technology. Future improvements to acqui-

sition technology for time-lapse monitoring, such as permanently deployed sensors or sea-bottom cable systems could be used to reduce the measurement uncertainties, particularly those associated with navigation of the transmitter, to well below 1%, making this 2D anomaly an appreciable target for monitoring purposes.

It is worth noting that during these time-lapse surveys cumulatively 1.33 and 2.29 million stock tank barrels (STB) of oil and 1.1 and 1.89 million standard cubic feet (MSCF) of gas is produced due to injection of 1.44 and 2.9 million STB of water after five and ten years, respectively. This information in conjunction with other parameters, e.g., reservoir depth, water depth, reservoir lithology type, oil-gas-water electrical properties, etc., can be used to develop criteria for detectability of other reservoirs located at comparable conditions.

The results presented here suggest that for a realistic reservoir to be monitored at a short time lag, i.e., less than five years, a data repeatability of much less than 1% is required for the basic CSEM measurements. As reported by [Orange et al. \(2009\)](#), this is likely to be impractical using the current CSEM technology that employs free-falling receivers and towed streamers. Besides, several other factors could obscure the small time-lapse signals. Some of the major considerations are errors in navigation of transmitters and receivers, an inhomogeneous near surface, effects of time-varying ocean conductivity, and changes in onsite field instruments and their sensor calibration corrections during production. All these issues have to be addressed and appropriately modeled to make time-lapse CSEM applicable for shorter time intervals through the reservoir's life.

Our 2D study is a first step in the direction of modeling the effects of exquisitely detailed reservoir production scenarios; however, it is worth considering how the 2D results are relevant for finite-length

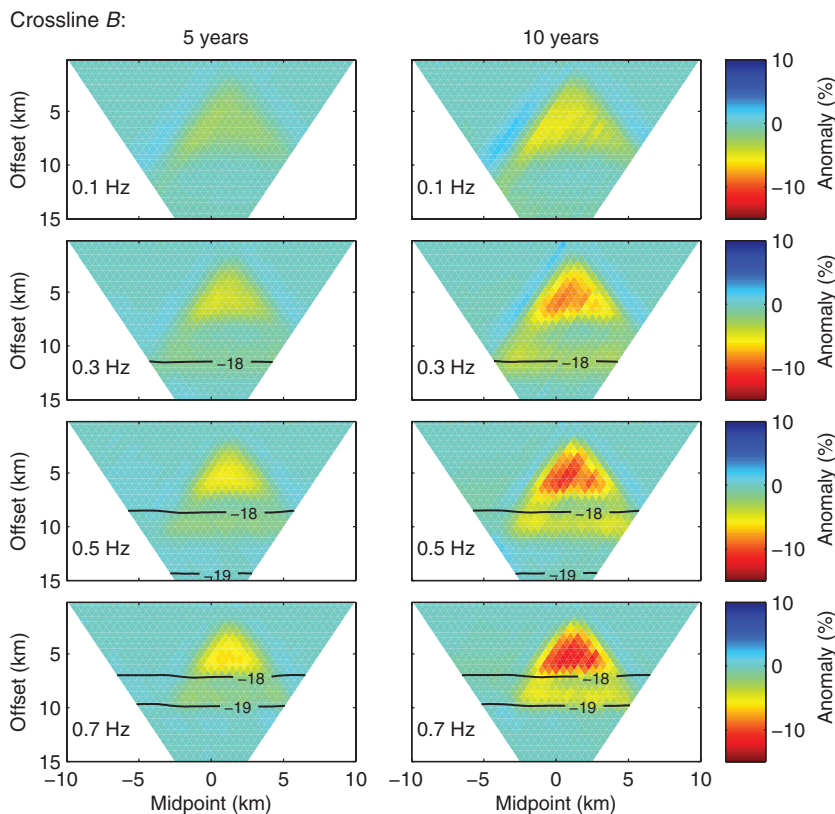


Figure 12. CSEM time-lapse responses computed for the crossline magnetic field as a function of frequency after five years (left column) and ten years (right column) of water flooding. Anomalies are computed as the relative difference between the water-flooded reservoir and the unflooded base reservoir. Anomalies are shown as a function of the transmitter-receiver midpoint and transmitter-receiver offset. Only positive offsets (transmitter to the right of the receiver) are shown. Black lines show amplitude contours at 10^{-18} and 10^{-19} T/Am, which roughly correspond to the system noise levels of existing CSEM instrumentation.

Figure 13. CSEM time-lapse responses computed for the inline horizontal electric field as a function of frequency after five years (left column) and ten years (right column) of water flooding. Black lines show amplitude contours at 10^{-15} and 10^{-16} V/Am², which roughly correspond to the system noise levels of existing CSEM instrumentation.

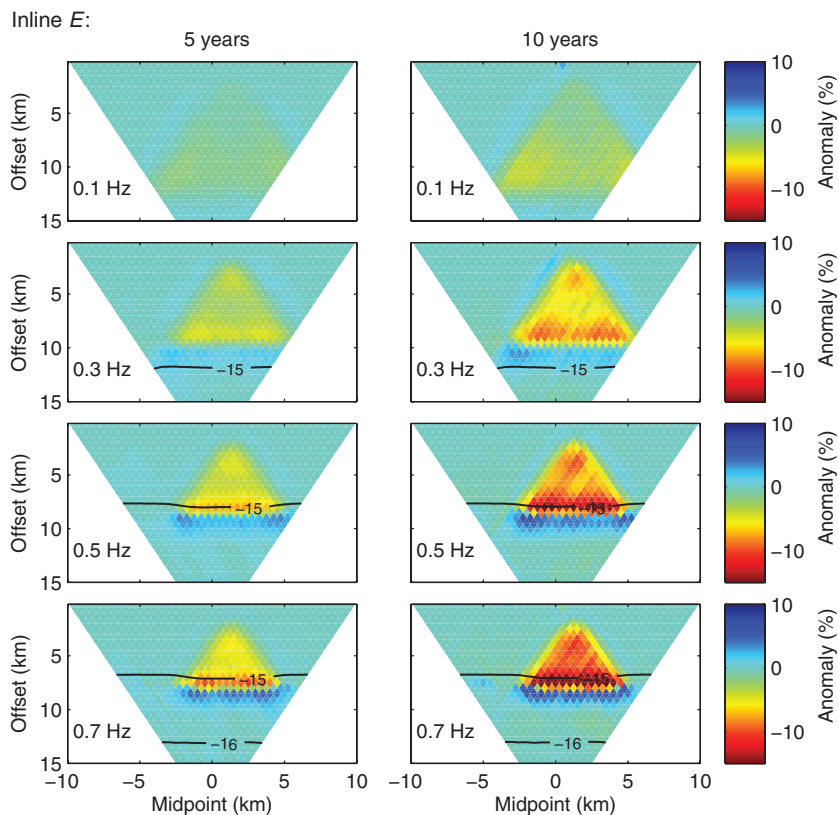
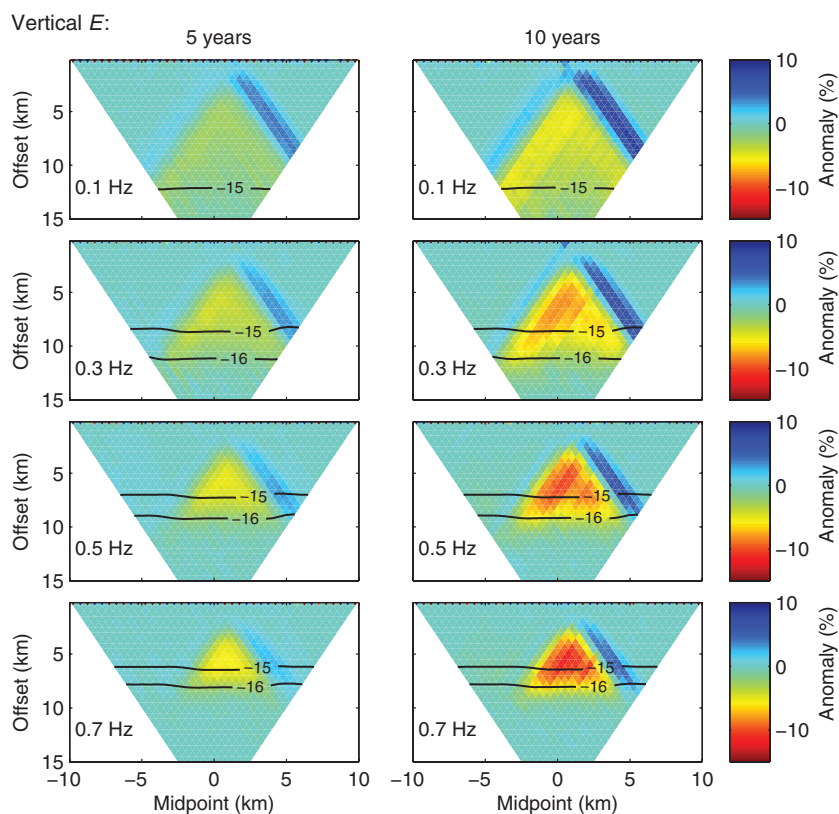


Figure 14. CSEM time-lapse responses computed for the vertical electric field as a function of frequency after five years (left column) and ten years (right column) of water flooding. Black lines show amplitude contours at 10^{-15} and 10^{-16} V/Am², which roughly correspond to the system noise levels of existing CSEM instrumentation.



3D reservoirs. Constable (2010) performed a 3D resolution kernel study that showed the region of highest CSEM sensitivity is largely confined to a narrow vertical zone between the source and receiver. While certainly there will be cases where 3D modeling is essential, this narrow sensitivity region suggests that the results from our 2D study will be relevant to 3D reservoirs as long as the survey profile spans the middle of an elongate 3D reservoir. Another concern is that the small-scale 3D heterogeneity within the reservoir and the 3D changes during production have not been captured by the 2D modeling scenarios. While such issues are best addressed by future 3D model studies of similarly detailed reservoirs, we expect that the volume averaging of the EM fields will likely act to smooth the effects of this variability, so that 3D time-lapse responses will be similar to the 2D responses when the survey profile is over the region where the largest changes in resistivity occur; for example, between the injection and production wells.

CONCLUSIONS

The geologically consistent petroelectric model developed in this paper explicitly relates petrophysical properties to rock resistivity. As a model, it can be generalized to other geological scenarios and, ultimately, applied to quantitative CSEM reservoir characterization and monitoring.

Our example application simulated three sets of 2D resistivity models corresponding to the initial reservoir state, and after five and ten years of water flooding of a 2200-m wide by 350-m thick oil reservoir. In these intervals, time-lapse changes in effective water saturation led to -20% – 60% decreases in electrical resistivity. A base and two monitor CSEM surveys were simulated via a highly accurate 2.5D adaptive finite element algorithm numerical algorithm. The CSEM responses show a 1%–5% time-lapse signal after five years and a stronger 5%–10% time-lapse signal after ten years of water flooding. Although small, these changes could be detected with the careful application of currently available CSEM acquisition technology. Signal levels at much shorter time intervals (a year or less) would be significantly smaller and not possible to detect with existing nodal CSEM receivers and deep-towed transmitters. Furthermore, factors restricting the repeatability of CSEM measurements, e.g., errors in positioning of transmitters and receivers, inhomogeneities in the near surface, effect of time-varying ocean conductivity, and changes in field instruments during production have to be addressed properly to preserve these relatively small time-lapse signals. Finally, more detailed and 3D time-lapse CSEM synthetic modeling and inversion, as well as time-domain CSEM simulation may shed light on complications probably not seen in our 2.5D frequency domain analyses.

ACKNOWLEDGMENTS

We would like to thank the sponsors of the UT-Austin EDGER Forum and the Jackson School of Geosciences at the University of Texas at Austin for their support of this research. K. Key was supported by the Seafloor Electromagnetic Methods Consortium at Scripps Institution of Oceanography. Alireza Shahin sincerely thanks Carlos Verdin, Jack Dvorkin, Larry Lake, and William Galloway for enlightening discussion on reservoir modeling. Special thanks to Anton Ziolkowski and three reviewers for critically reviewing the manuscript and suggesting many improvements. A note of special gratitude goes to Schlumberger for providing reservoir

simulation software. The San Diego Supercomputer Center at UCSD provided access to the Triton Compute Cluster.

APPENDIX A

PETROPHYSICS AND ROCK-FLUID PHYSICS MODEL TO COMPUTE ELECTRICAL RESISTIVITY

As described in the petrophysics model, the clay distribution is dispersed or pore-filling. The corresponding porosity-clay model was introduced by Thomas and Stieber (1975) and further developed by Marion et al. (1992). Total φ_t and effective φ_e porosity in shaly sand domain is calculated as follows

$$\varphi_t = \varphi_{ss} - C_{sh}(1 - \varphi_{sh}) \quad C_{sh} \leq \varphi_{ss} \quad (\text{A.1})$$

$$\varphi_e = \varphi_t - \varphi_{sh}C_{sh} \quad (\text{A.2})$$

where φ_{sh} is pure shale porosity, φ_{ss} is the clean sandstone porosity, and C_{sh} is the volumetric shale concentration of the rock.

Dual water models (Best, 1980; Dewan, 1983; Clavier, 1984) are applicable for dispersed clay distributions. In this study, we use the dual water model because several of its parameters can be computed from well logs (Dewan, 1983) and it can be efficiently combined with the dispersed clay model. Based on this model, electrical-conductivity or inverse of rock resistivity (R_t) is computed as follows

$$\frac{1}{R_t} = \frac{\varphi_t^m S_{wt}^n}{a} \left[\frac{1}{R_w} + \frac{S_{wb}}{S_{wt}} \left(\frac{1}{R_{wb}} - \frac{1}{R_w} \right) \right] \quad (\text{A.3})$$

Where a , m , n are tortuosity factor, cementation factor, and saturation exponent, respectively, S_{wb} and S_{wt} are clay bound-water saturation and total water saturation, respectively and are computed using

$$S_{wb} = \frac{C_{sh}\phi_{sh}}{\phi_t} \quad (\text{A.4})$$

$$S_{wt} = S_{wb} \frac{S_{ws}\phi_e}{\phi_t} \quad (\text{A.5})$$

The terms R_w and R_{wb} are free and bound-water resistivity which depends on salinity and temperature. We use Arps' empirical equation (Arps, 1953) to calculate these quantities:

$$R_w = \left[0.0123 + \frac{3647.5}{\text{NaCl}(\text{ppm})^{0.995}} \right] * \left[\frac{81.77}{T(\text{oF}) + 6.77} \right] \quad (\text{A.6})$$

Where the concentration of NaCl in particle per million (ppm) and temperature (T) in Fahrenheit degree are required to compute fluid resistivity.

REFERENCES

- Archie, G. E., 1942, The electrical resistivity of log as an aid in determining some reservoir characteristics: *Petroleum Transactions, AIME*, **146**, 54–61.
- Arps, J. J., 1953, The effect of temperature on the density and electrical resistivity of sodium chloride solutions: *Petroleum Transactions, AIME*, **198**, 327–328.
- Avseth, P., T. Mukerji, and G. Mavko, 2005, *Quantitative seismic interpretation*: Cambridge University Press.
- Aziz, K., and A. Settari, 1979, *Petroleum reservoir simulation*: Applied Science Publishers LTD.
- Batzle, M., and Z. Wang, 1992, Seismic properties of pore fluids: *Geophysics*, **57**, 1396–1408, doi: [10.1190/1.1443207](https://doi.org/10.1190/1.1443207).
- Best, D. L., J. S. Gardner, and J. L. Dumanoir, 1980, A computer-processed wellsite log interpretation: *SPE*, 9039.
- Black, N., and M. S. Zhdanov, 2009, Monitoring of hydrocarbon reservoirs using marine CSEM method: 79th Annual International Meeting, SEG, Expanded Abstracts, 850–854.
- Christie, M. A., and M. J. Blunt, 2001, Tenth society of petroleum engineers comparative solution project: A comparison of upscaling techniques: *Reservoir Simulation Symposium, SPE*, 72469.
- Clavier, C., G. Coates, and J. Dumanoir, 1984, Theoretical and experimental bases for the dual water model for interpretation of shaly sands: *SPE* 6859.
- Constable, S., 2010, Ten years of marine CSEM for hydrocarbon exploration: *Geophysics*, **75**, no. 5, 75A67–75A81, doi: [10.1190/1.3483451](https://doi.org/10.1190/1.3483451).
- Constable, S., and L. J. Srnka, 2007, An introduction to marine controlled-source electromagnetic methods for hydrocarbon exploration: *Geophysics*, **72**, WA3–WA12, doi: [10.1190/1.2432483](https://doi.org/10.1190/1.2432483).
- Constable, S., and C. J. Weiss, 2006, Mapping thin resistors and hydrocarbons with marine EM methods: Insights from 1D modeling: *Geophysics*, **71**, no. 2, G43–G51, doi: [10.1190/1.2187748](https://doi.org/10.1190/1.2187748).
- Dewan, J. T., 1983, *Essentials of modern open-hole log interpretation*: PennWell Books.
- Dvorkin, J., and M. Gutierrez, 2002, Grain sorting, porosity, and elasticity: *Petrophysics*, **43**, 185–196.
- Dvorkin, J., G. Mavko, and B. Gurevich, 2007, Fluid substitution in shaly sediments using effective porosity: *Geophysics*, **72**, no. 3, O1–O8, doi: [10.1190/1.2565256](https://doi.org/10.1190/1.2565256).
- Eidesmo, T., S. Ellingsrud, L. M. MacGregor, S. Constable, M. C. Sinha, S. Johansen, F. N. Kong, and H. Westerdahl, 2002, Seabed logging (SBL), a new method for remote and direct identification of hydrocarbon filled layers in deepwater areas: *First Break*, **20**, 144–152.
- Ellingsrud, S., T. Eidesmo, S. Johansen, M. C. Sinha, L. M. MacGregor, and S. Constable, 2002, Remote sensing of hydrocarbon layers by seabed logging (SBL): Results from a cruise offshore Angola: *The Leading Edge*, **21**, 972–982, doi: [10.1190/1.1518433](https://doi.org/10.1190/1.1518433).
- Galloway, W. E., and D. K. Hobday, 1996, *Terrigenous clastic depositional systems: Applications to fossil fuel and groundwater resources*, 2nd edition, Springer-Verlag.
- Hacikoylu, P., J. Dvorkin, and G. Mavko, 2006, Resistivity-velocity transforms revisited: *The Leading Edge*, **25**, 1006–1009, doi: [10.1190/1.2335159](https://doi.org/10.1190/1.2335159).
- Hoversten, G. M., F. Cassassuce, E. Gasperikova, G. A. Newman, J. Chen, Y. Rubin, Z. Hou, and D. Vasco, 2006, Direct reservoir parameter estimation using joint inversion of marine seismic AVA and CSEM data: *Geophysics*, **71**, no. 3, C1–C13, doi: [10.1190/1.2194510](https://doi.org/10.1190/1.2194510).
- Key, K., 2009, 1D inversion of multicomponent, multifrequency marine CSEM data: Methodology and synthetic studies for resolving thin resistive layers: *Geophysics*, **74**, F9–F20, doi: [10.1190/1.3058434](https://doi.org/10.1190/1.3058434).
- Key, K., and J. Oval, 2011, A parallel goal-oriented adaptive finite element method for 2.5D electromagnetic modeling: *Geophysical Journal International*, **186**, 137–154, doi: [10.1111/gji.2011.186.issue-1](https://doi.org/10.1111/gji.2011.186.issue-1).
- Killough, J. E., 1995, Ninth SPE comparative solution project: A reexamination of black-oil simulation: *SPE Reservoir Simulation Symposium*, **29110**, 135–147.
- Li, Y., and K. Key, 2007, 2D marine controlled-source electromagnetic modeling: Part 1 — An adaptive finite-element algorithm: *Geophysics*, **72**, WA51–WA6, doi: [10.1190/1.2432262](https://doi.org/10.1190/1.2432262).
- Lien, M., and T. Mannseth, 2008, Sensitivity study of marine CSEM data for reservoir production monitoring: *Geophysics*, **73**, no. 4, F151–F163, doi: [10.1190/1.2938512](https://doi.org/10.1190/1.2938512).
- Marion, D., A. Nur, H. Yin, and D. Han, 1992, Compressional velocity and porosity in sand-clay mixtures: *Geophysics*, **57**, 554–563, doi: [10.1190/1.1443269](https://doi.org/10.1190/1.1443269).
- Myer, D., S. Constable, and K. Key, 2011, Broad-band waveforms and robust processing for marine CSEM surveys: *Geophysical Journal International*, **184**, 689–698, doi: [10.1111/gji.2011.184.issue-2](https://doi.org/10.1111/gji.2011.184.issue-2).
- Orange, A., K. Key, and S. Constable, 2009, The feasibility of reservoir monitoring using time-lapse marine CSEM: *Geophysics*, **74**, no. 2, F21–F29, doi: [10.1190/1.3059600](https://doi.org/10.1190/1.3059600).
- Revil, A., and L. M. Cathles, 1999, Permeability of shaly sands: *Water Resources Research*, **35**, 516–662, doi: [10.1029/98WR02700](https://doi.org/10.1029/98WR02700).
- Saner, S., M. N. Cagatay, and A. M. Al Sanounah, 1996, Relationships between shale content and grain-size parameters in the Safaniya sandstone reservoir, NE Saudi Arabia: *Journal of Petroleum Geology*, **19**, 3, 305–320, doi: [10.1111/jpg.1996.19.issue-3](https://doi.org/10.1111/jpg.1996.19.issue-3).
- Shahin, A., P. L. Stoffa, R. H. Tatham, and R. Seif, 2011, Accuracy required in seismic modeling to detect production-induced time-lapse signatures: 81st Annual International Meeting, SEG, 2860–2864.
- Shahin, A., R. H. Tatham, P. L. Stoffa, and K. T. Spikes, 2010, Comprehensive petro-elastic modeling aimed at quantitative seismic reservoir characterization and monitoring: 80th Annual International Meeting, SEG, Expanded Abstracts, 2245–2250.
- Thomas, E. C., and S. J. Stieber, 1975, The distribution of shale in sandstones and its effect upon porosity, paper T in the 16th Annual Logging Symposium Transactions: Society of Professional Well Log Analysts.
- Tyler, N., and W. A. Ambrose, 1986, Facies architecture and production characteristics of strand-plain reservoirs on north Markham-North Bay City Field, Frio formation, Texas: *AAPG Bulletin*, **70**, 809–829.
- Uden, R., J. Dvorkin, J. Walls, and M. Carr, 2004, Lithology substitution in a sand/shale sequence, Extended Abstracts, ASEG 17th Geophysical Conference and Exhibition, Sydney.
- Um, E. S., and D. L. Alumbaugh, 2007, On the physics of the marine controlled-source electromagnetic method: *Geophysics*, **72**, no. 2, WA13–WA26, doi: [10.1190/1.2432482](https://doi.org/10.1190/1.2432482).
- Waxman, M. H., and L. J. M. Smits, 1968, Electrical conductivities in oil-bearing shaly sands: *SPE Journal*, **8**, 107–12, doi: [10.2118/1863-A](https://doi.org/10.2118/1863-A).
- Wright, D., A. Ziolkowski, and B. Hobbs, 2002, Hydrocarbon detection and monitoring with a multicomponent transient electromagnetic (MTEM) survey: *The Leading Edge*, **21**, 852–864, doi: [10.1190/1.1508954](https://doi.org/10.1190/1.1508954).
- Zach, J. J., M. A. Frenkel, D. Ridyard, J. Hincapie, B. Dubois, and J. P. Morten, 2009, Marine CSEM time-lapse repeatability for hydrocarbon field monitoring: 79th Annual International Meeting, SEG, Expanded Abstracts, 820–823.
- Ziolkowski, A., R. Parr, D. Wright, V. Nockles, C. Limond, E. Morris, and J. Linfoot, 2010, Multi-transient electromagnetic repeatability experiment over the North Sea Harding field: *Geophysical Prospecting*, **58**, no. 6, 1159–1176.